Structural and chemical investigation of interface related magnetoelectric effect in Ni/BiFe0.95Mn0.05O3 heterostructures

B. Negulescu, J. Wolfman, Christophe Daumont, Nazir Jaber, Pascal Andreazza, Thibaud Denneulin, Sylvie Schamm-Chardon

Structural and chemical investigation of interface related magnetoelectric effect in Ni / $BiFe_{0.95}Mn_{0.05}O_3$ heterostructures

B. Negulescu[1,&], J. Wolfman[1], C. Daumont[1], N. Jaber[1], P Andreazza[2], T. Denneulin[3,4,5], S. Schamm-Chardon[4,5]

[1] GREMAN, UMR 7347, Université de Tours, CNRS, Parc de Grandmont 37200 Tours, France

[2] ICMN, UMR7374, Université d'Orléans, CNRS, Rue de la Férollerie, 45071 Orléans, France

[3] Ernst Ruska-Centre for Microscopy and Spectroscopy with Electrons and Peter Grünberg Institute, Forschungszentrum Jülich, Jülich 52425, Germany

[4] CEMES CNRS, 29 Rue Jeanne Marvig, F-31055 Toulouse, France

[5] Université de Toulouse, 29 Rue Jeanne Marvig, F-31055 Toulouse, France

& e-mail: beatrice.negulescu@univ-tours.fr

Abstract

The magnetoelectric coupling mechanism in Ni / $BiFe_{0.95}Mn_{0.05}O_3$ heterostructures is investigated through a detailed microstructural study of the $BiFe_{0.95}Mn_{0.05}O_3$ film and a chemical analysis of the Ni/ $BiFe_{0.95}Mn_{0.05}O_3$ interface. The four structural variants expected in BiFe0.95Mn0.05O3 are detected by high resolution X-ray diffraction reciprocal space mapping method. The ferroelectric domain structure is imaged with transmission electron microscopy. Oxidized Ni is evidenced at the Ni/ $BiFe_{0.95}Mn_{0.05}O_3$ interface by electron energy

loss spectroscopy and X-ray photoemission spectroscopy, although the degree of Ni oxidation is independent of the magnetoelectric state of the heterostructure.

1. Introduction

The electric field control of the magnetic state in spintronic devices has the benefit to eliminate the need for large current densities, thus decreasing Joule heating and power consumption [1], [2]. To realize such devices, ferromagnetic / ferroelectric thin film heterostructures are prime candidates due to their compatibility with the Si technology [3], [4], [5], [6]. In these heterostructures different mechanisms allowing for the electrical manipulation of magnetism have been proposed, such as strain variation in the ferromagnetic layer induced by inverse piezoelectric effect, interfacial charge modulation driven by ferroelectric polarization switching, or exchange coupling with an antiferromagnetic multiferroic material [1], [7]. Electrochemical effects, mainly related to oxygen ions migration in electric field, can be added to these three main mechanisms [8], [9], [10].

In a previous paper we have reported a strong magnetoelectric coupling in Ni/ $BiFe_{0.95}Mn_{0.05}O_3$ (BFMO) heterostructure [11] that shows a large modulation of the magnetic properties of the Ni layer induced by the ferroelectric polarization switching of the BFMO film. The repeatability of the effect, demonstrated up to several hundreds of switching cycles, makes this system promising for future applications. In this paper we present a detailed structural and chemical analysis of the Ni/ BFMO heterostructure aiming to disentangle between the different coupling mechanisms.

2. Experimental details

$La_{0.8}Sr_{0.2}MnO_3$ (25 nm) / $BiFe_{0.95}Mn_{0.05}O_3$ (60nm) thin films were deposited on (110)-oriented $GdScO_3$ substrates using pulsed laser deposition at a substrate temperature of 700°C in an oxygen pressure of 0.2mbar and a laser fluence of about $2J.cm^{-2}$. The conductive $La_{0.8}Sr_{0.2}MnO_3$ (LSMO) layer is used as a bottom electrode. For the magnetoelectric measurements Ni (30nm)/Au (10nm) top electrodes were deposited by e-beam evaporation using a lift-off process. A special sample was fabricated for X ray photoelectron spectroscopy measurements using Ni (3nm)/Au (3nm) top electrodes.

The magnetoelectric effect was studied using a Durham Magneto Optics NanoMOKE magnetometer for the hysteresis cycles measurements coupled with a Keithley 2410 Source Meter for the electric field.

The chemical and structural characterization of the heterostructure was performed by different techniques using X-rays and electron beams: high resolution X-ray diffraction Reciprocal Space Mapping (RSM), X-ray Photoemission Spectroscopy (XPS), High Resolution Transmission Electron Microscopy (HRTEM), Electron Energy-Loss Spectroscopy (EELS), Selected Area Electron Diffusion (SAED) and Dark-Field Electron Holography (DFEH). X-ray diffraction (XRD) was realized with a Cu Kα1 parallel beam using a Bruker 4-circles D8 Discover system. The XPS spectra were recorded in a ULVAC-PHI Versaprobe 2 spectrometer using a monochromatic Al Kα source (1486.6eV at 4.4W). The charge neutralizer working at 1V and 20µA was employed with combined electrons and ions during all scans. For the survey scans, an 1100–0 eV energy range was used with 187.85eV pass energy. The high resolution scans were measured using 23.50eV pass energy, 0.2eV step and 60s sweep intervals. Peak shifts were corrected using the $Au4f_{7/2}$ peak at 84eV.

For the TEM-based analyses, TEM lamellae were thinned down to 100-150nm with a FEI Helios Nanolab 600 focused ion beam operated at 30kV, followed by low 5kV voltage ion

polishing. High Resolution imaging was performed with a field emission aberration-corrected transmission electron microscope (FEI Tecnai F20) operating at 200 kV. The 1nm focused probe of the microscope can be scanned over the area of interest while an imaging filter (Gatan GIF Tridiem) is used as a spectrometer for local EELS studies. SAED patterns, dark-field images and dark-field electron holograms were obtained using a Hitachi HF-3300 TEM equipped with a cold field emission gun operated at 300kV (more details in the supplementary material).

3. Results and discussions

3.1. Magnetoelectric properties

The magnetoelectric effect was studied by measuring the in-plane magnetic hysteresis cycles of the top Ni electrode while applying a DC voltage between the top and the bottom electrodes. Figure 1 (a) shows the hysteresis cycles obtained in zero electric field for the as deposited state and after different poling sequences. In the as deposited state, the Ni film exhibits a small coercive field Hc=20Oe (black curve). After switching the ferroelectric polarization in positive voltage, the magnetic coercive field increases to 180Oe. This magnetic state is stable after removing the electrical field (red curve). In negative bias the reversal of the ferroelectric polarization induces a decrease of the magnetic coercive field compared to the positive bias and again this magnetic state is stable upon electric field removal (blue curve). After the negative bias sequence the 60Oe coercive field is 3 times larger than the as-deposited one, indicating that the initial state is no longer recovered. Nevertheless, the switching between the low magnetic coercive state and the high one is repeatable [11]. Also noticeable in Fig. 1(a) is the 15 % variation of the saturation magnetization associated with the modulation of the magnetic coercive field.

The typical current – voltage (I-V) curve presented in Fig 1(b) is characterized by asymmetric leakage currents under positive/negative bias voltage, induced by the asymmetric electrode structure. The current density is 4mA/cm^2 at 2V while it increases up to 40mA/cm^2 at -2V (electrode area 50x50µm^2). The small current peak observed in positive bias voltage when coming from -2V (arrow in Fig. 1(b)) indicates the polarization reversal, whereas its signature is hidden in the negative bias domain by the rectifying behavior of the structure. Nevertheless, the hysteresis observed in the negative bias region results from the ferroelectric character of the BFMO film [12], [13], [14].

Being associated with the ferroelectric polarization reversal, the modulation of the magnetic properties could be induced either by charge effects or by the coupling of the antiferromagnetic structure of BFMO with the ferromagnetic Ni structure [11]. Besides, ion migration under electric field could modify the composition of the BFMO film at the interface or oxidize the Ni film. In order to understand the magnetoelectric coupling mechanism in the Ni/BFMO heterostructure and to distinguish between these different coupling mechanisms, two different types of investigation have been conducted. First, a detailed study of the ferroelectric structure in the BFMO layer was carried out to detect eventual specific features in the polarization reversal and domain configuration that could relate to the magnetic coercive field modulation [15], [16], [44]. Second, the interfacial chemical state was investigated in search of an eventual oxidation of the Ni film induced by voltage driven oxygen migration, as demonstrated in some recent publications [8], [9], [10].

3.2. Structural properties

Complementary XRD and TEM crystallographic analyses were performed, in particularly looking for the domain structure in the BFMO layer. Let us consider $BiFeO_3$ (BFO) as crystallographically representative of our $BiFe_{0.95}Mn_{0.05}O_3$. Bulk BFO is rhombohedral with a pseudo cubic lattice parameter a_{pc}=3.965Å, though in epitaxial thin films a lowering of the crystal symmetry towards a monoclinic structure is generally observed due to strain effects [17], [18]. The lattice constants of the orthorhombic $GdScO_3$ (GSO) substrate are a_o=5.48Å, b_o=5.75Å, and c_o=7.93Å [19]. In this structure, the $(110)_o$ planes provides a nearly square base with $c_o/2$=3.966 Å and sqrt(a_o+b_o)/2=3.970Å, which gives an average 0.1% misfit strain with BFO. Epitaxial growth of BFO films with a controlled domain configuration was achieved on GSO [20], [21], the ferroelectric structure being very sensitive to the growth quality of the bottom electrode [20], [22].

The crystalline quality of the epitaxial BFMO films was studied by XRD before the deposition of the top electrodes. The RSMs around the $(\pm103)_{pc}$ and $(0\pm13)_{pc}$ asymmetric reflections are shown in Fig. 2(a - d). With the pseudo cubic notation used here, the equivalence between the GSO orthorhombic and pseudo cubic structure is given by: $[001]_o$ = $[100]_{pc}$, $[1\text{-}10]_o$= $[010]_{pc}$ and $[110]_o$ = $[001]_{pc}$. In the RSMs, the highest intensity reflections are assigned to the substrate and the less intense ones to the BFMO film (LSMO reflections do not appear as Qz_{LSMO}>7.73nm^{-1}). Due to the orthorhombic structure of the GSO substrate, the corresponding peaks appear in different positions from one map to another. Also, a splitting of the BFMO peak can be observed in all maps, which signs the presence of all four possible structural domains [20], [22]. The peaks corresponding to the BFMO film and substrate are not vertically aligned: the GSO peak appears at Qx(y)=2.52nm^{-1} while the BFMO peaks are shifted towards higher Qx(y) values. This shift, observed in all four maps in Fig. 2, indicates a smaller in plane lattice parameter for the BFMO layer than the one of the GSO substrate. As

the BFMO peaks are quite large it is difficult to define precisely the lattice parameters, but the value stands between 3.94Å and 3.95Å. This observed decrease of the in plane BFMO lattice parameter results from the strain imposed by the 25 nm LSMO buffer layer, which should be at least partially relaxed due to the large lattice mismatch with the GSO substrate (the bulk pseudo cubic lattice parameter of LSMO is 3.88Å [23], [24]).

Fig. 3(a) presents a conventional TEM image of the whole stack showing sharp interfaces. On the SAED in Fig. 3(b), the intense and less intense arrays of diffraction spots correspond to the contributions of the BFMO/LSMO layers and the substrate, respectively. The single crystalline structure of the BFMO film is thus confirmed. The weak spotty ring pattern is the signature of the polycrystalline Ni (Au) film. The zoom in the bottom left inset of Fig. 3(b) highlights the splitting between the high order spots of the substrate (blue) and the layers (red). This is due to the orthorhombic structure of the GSO substrate that has a 92.7° angle between the $(001)_{pc}$ and $(010)_{pc}$ lattice planes [19].

The dark field TEM images obtained with the $(002)_{pc}$ and $(00\text{-}2)_{pc}$ GSO diffracted beams are shown in Fig. 3 (c) and (d) for two regions of the sample: one that was not switched under electric field (c), denoted as un-poled, and another that was electrically switched several times (d), denoted as poled. In Fig. 3(d) the alternation of bright/dark regions along the BFMO layer for each diffracted beam and the inversion of the contrast going from one dark-field image to the other (top versus bottom) reveal the presence of ferroelectric domains with different orientations [25]. The domains are separated by either vertical or inclined walls (pointed by yellow arrows), corresponding probably to 109° and 180° (or 71°) ferroelectric domain walls (DW), respectively [20], [21], [26], [27]. Such a sharp domain contrast is not observed in the un-poled sample (Fig. 3(c)). This could be due to a smaller size of the as deposited ferroelectric domains than the thickness of the TEM lamella (100 – 150 nm thick), therefore leading to a

superposition of domains through the lamella. Another possibility would be that in all the domains the polarization of the as-deposited BFMO film is pointing towards the bottom electrode, as generally observed in these epitaxial structures [22], [28], [29], thus generating no contrast in Fig. 3(c).

DFEH measurements were realized in order to get more information about the strain state of the film [30]. Fig. 4(a) shows a dark-field hologram using the $(00\text{-}2)_{pc}$ GSO diffracted beam of the same poled region presented in Fig. 3(d), where ferroelectric domains separated by inclined and vertical DW (indicated by the arrows A and B for instance) appear. Fig. 4 (b) and (c) show the reconstructed vertical deformation map and rotation map of the $(002)_{pc}$ lattice planes. The deformation is defined as : $\varepsilon = (d_{(x,y)} - d_{GSO}) / d_{GSO}$ with d_{GSO} being the $(002)_{pc}$ interplanar distance in the GSO substrate and d(x,y) being the $(002)_{pc}$ interplanar distance at any position (x,y) in the deformation map. The rotation is also defined with respect to the lattice planes of the substrate (zero rotation means that the planes are parallel to the substrate) and it is clockwise positive. The spatial resolution in the reconstructed maps is 7nm and the precision is +/-0.05% for the deformation and +/-0.03° for the rotation. The deformation is negative in the bottom electrode (about -1%) because LSMO has a smaller out-of-plane lattice parameter than GSO. The deformation in the BFMO layer is less uniform than in the LSMO layer and has an average value of -0.2%. Moreover, the rotation map shows significant positive / negative deviations when crossing the vertical DWs. The line profile in Fig. 4(d), extracted along the dashed black line in Fig. 4(c), shows variations from -0.5° to +0.5° in a short lateral range (about 20nm) around the vertical DWs (see for instance the region noted B). Interestingly, the rotation of the planes relaxes inside the domain, away from the wall, (for instance in the regions C and D, about 80nm from B). The rotation map remains uniform around the inclined DWs in region A.

Using the r1 – r4 notation of the four rhombohedral domain variants presented in Fig. 4 (e), schematics of possible domain arrangement are presented in Fig. 4 (f) and (g). The inclined DW noted A in Fig. 4(a, c) is probably a 180° DW, separating r_2^+ / r_2^- domains (or equivalently r_3^+ / r_3^-). The orientation of the structure does not change, but only the direction of the polarization. The vertical DW B is probably a 109° DW, separating r_2^- / r_1^+ (or r_3^- / r_4^+) domains. In this case, the inclination of the structure changes [31] as indicated in Fig. 4(g) by small tilts of +/- ω of the BFMO $(001)_{pc}$ planes, with respect to the substrate. In BFO structure, the rhombohedral distortion angle α being 89.4° [32], the expected tilt angle is ω =0.6°, which is close to the maximum rotation measured near the vertical walls. In the regions C and D away from the DW, the $(001)_{pc}$ planes of the BFMO film and substrate are parallel (ω =0), as shown schematically in Fig. 4(h).

To conclude on the crystallographic analysis of the BFMO structure, all four structural variants of the BFMO film are present, leading to a mosaic-like ferroelectric domain structure (presented in our previous article [11]). Related to this domain structure, all types of DW are expected [33], even though no 71° DW were detected in our TEM analysis. As demonstrated in BFO/ CoFe heterostructure, the presence of 109° DWs induces an exchange bias effect [33], [34], [43] when the CoFe film is deposited in magnetic field. In our samples the Ni film was deposited without any magnetic field and no exchange bias was observed. In parallel, the coupling between antiferromagnetic BFO and ferromagnetic films has been shown to induce an enhancement of the magnetic coercive field [33], [34], [43]. We observed a rather weak (3Oe) enhancement of the Ni coercive field going from Ni/GSO to Ni/BFMO/GSO heterostructure (Fig. S1 in supplementary material) which could be ascribed to the BFMO top surface roughness. This result indicates the negligible contribution of the ferromagnetic /

antiferromagnetic coupling in our Ni/BFMO structure, as it was already shown in the closely related Ni/ BFO system [45].

However, in order to conclude about the role of the ferroelectric domain configuration in the magnetoelectric effect, one should compare the ferroelectric structure in poled and un-poled states. Unfortunately our TEM analysis could not clearly establish the domain structure of un-poled BFMO structure due to the lack of contrast in the dark field TEM images.

3.3. Interfacial chemistry

The interfacial chemistry of the Ni/ BFMO heterostructure has been investigated by EELS and XPS. Figure 5 shows HRTEM images of the Ni/BFMO interface for two different electric states: un-poled (Fig. 5(a)) and poled by several electric field cycles (Fig. 5 (b)). Both images show a transition from a single crystalline structure in BFMO to a polycrystalline one in the Ni film, however a small difference between the two states can be distinguished at the Ni/BFMO interface. In the poled region an ordered structure of 1-2nm thick appears between the epitaxial BFMO film and the polycrystalline Ni (see yellow lines fig (5b)), which might be associated to a secondary phase. Nevertheless, this interfacial ordered structure does not appear in all the HRTEM images of the poled region.

Electron energy loss spectra elementary profiles determined from the oxygen K (O-K), iron L (Fe-L) and nickel L (Ni-L) edges acquired across the interfaces of the un-poled and poled samples are shown in Fig. 5 (c) and (d), respectively. For both states, a few nanometer thick interfacial region where the three signatures are simultaneously present can be defined, indicating either an interfacial roughness or a chemical mixing. The study of the O-K edge fine structures shows that the O-K signature at the Ni/BFMO interface has similar features than the one observed in NiO [35], [36] whereas the O-K measured 15nm away from the interface

in the BFMO layer is, as expected, typical for BFO (Fig. 5 (e)) [37], [38], [39]. This clearly indicates a local Ni oxidation at the interface with BFMO. The spatial extent of the Ni oxide has been estimated by simulating the O-K energy-loss near-edge structure (ELNES) across the interface with a linear combination of the BFMO and NiO references. In Fig. 5 (c) and (d), the O-K elementary profile is thus split in two contributions, one representative of O-K in BFMO (dashed) and the other representative of O-K in NiO (dotted). A similar increase of the O-K NiO signal over 3-4nm is observed at the interface for both poled and un-poled regions indicating a negligible influence of the electric field on the oxygen migration.

XPS experiments were also performed in order to check for a possible ionic migration induced by the electric field. For these measurements a special electrode configuration was fabricated using thinner metallic films, Ni 3nm covered by 3nm Au, and electrodes of 100x100μm^2 area. Some of the electrodes were used to pole the BFMO underneath and induce a high magnetic coercive state in Ni, while other electrodes were left in the as-deposited state. To avoid any problem of charge or contamination, the sample surface was gently sputter cleaned before XPS measurements by Ar_n^+ gas cluster ion beam. The survey scan presented in Fig. 6(a) shows that besides the Au and Ni peaks, Bi and Fe were also detected, indicating that the measurement is sensitive to the BFMO / Ni interface. Figure 6(b) show the spatial distribution of the different elements with respect to the analysis region (18µm) used for high resolution measurements of the BFMO / Ni interface. Fig. 6(c) presents the high resolution Ni2$p_{3/2}$ core level spectra for the poled and un-poled regions. As already observed in the ELNES measurements, these spectra do not show any significant difference between the two electrical states.

Ni metal is characterized by a peak at 852.6eV with a satellite due to surface plasmon losses at +6eV and a less intense satellite peak at +3.7eV [40], [41]. However, it is not possible

to correctly fit the measured XPS spectra using only these 3 peaks. Additional loss peaks corresponding to Ni^{2+} at 854eV and 857eV [40], [41], [42] were needed to accurately fit the experimental spectra. The presence of Ni^{2+} in the experimental spectra confirms partial Ni oxidation as evidenced by ELNES. The fit obtained with this configuration for the poled region is presented in Fig. 6(c) and the fit parameters are shown in Table 1. A slightly higher Ni oxidation is obtained for the un-poled region, with 57.9 % area for the metallic Ni peak, 22.9% area for the Ni-oxide 1 and 9% for Ni-oxide 2 peaks.

Table 1: Fitting parameters for poled $Ni2p_{3/2}$ XPS spectra from Fig. 6 (d)

Spec	Band Position (eV)	Separation (eV)	FWHM	Height	%Gauss	Area	%Area
Ni^0	852.5	0	1.32	692	70	1431	62.1
Ni^0 satellite	856.2	3.7	1.7	19	70	39	1.7
Ni^0 plasmon	858.5	6	2.4	74	70	215	9.3
Ni oxide 1	854	1.5	3.0	133	80	466	20.2
Ni oxide 2	857	4.5	2.8	49	90	154	6.7

4. Conclusion

We report on the structural and chemical analysis of Ni / $BiFe_{0.95}Mn_{0.05}$ heterostructure that shows a large magnetoelectric effect. The electric field applied to the ferroelectric BFMO film modulates the magnetic coercive field of the Ni film through interfacial magnetoelectric coupling.

The high quality epitaxial growth of the BFMO film with four variants ferroelectric domain structure was demonstrated. The domain structure and the type of domain walls in the electrically poled BFMO regions were identified. Oxidized Ni at the BFMO / Ni interface was evidenced, the degree of Ni oxidation being independent on the electric field history of the

sample. The hypothesis of an oxygen ionic migration induced by the electric field is not sustained by this work.

Supplementary Material

See Supplementary Material for a detailed presentation of the TEM based experimental conditions and magnetic measurements of Ni(30nm) films deposited directly on GSO substrate and on BFMO film.

Acknowledgments

This work was financially supported by Région Centre, France, through Project COMHET (No. 2013 00082885).

References

[1] V. Garcia, M. Bibes, A. Barthélémy, C. R. Physique, 2015, 16, 168-181.

[2] F. Matsukura, Y. Tokura, H. Ohno, Nature Nanotechnology, 2015, 10 , 209-220.

[3] Z. Yu, Y. Liang, C. Overgaard, X.Hu, J. Curless, H. Li, Y. Wei, B. Craigo, D. Jordan, R. Droopad, J. Finder, K. Eisenbeiser, D. Marshall, K. Moore, J. Kulik, P. Fejes, Thin Solid Films 2004, 462–463, 51–56.

[4] R. Ramesh, N. A. Spaldin, Nature Materials, 2007, 6 , 21-29.

[5] R. Thomas, J. F. Scott, D. N. Bose, R. S. Katiyar, J. Phys.: Condens. Matter, 2010, 22, 423201.

[6] S-H Baek, C-B Eom, Acta Materialia, 2013, 61, 2734-2750.

[7] J.-M. Hu, L.-Q. Chen and C.-W. Nan, Adv. Mat. , 2016, 28, 15-39.

[8] U. Bauer, L. Yao, A.J. Tan, P. Agrawal, S. Emori, Harry L. Tuller, S. van Dijken, G.S.D. Beach, Nat. Mater. 2015, 14, 174-181.

[9] D.A. Gilbert, A.J. Grutter, E. Arenholz, K. Liu, B.J. Kirby, J.A. Borchers, B.B. Maranville, Nat. Comm., 2016, 7, 12264.

[10] X. Zhou, Y. Yan, M. Jiang, B. Cui, F. Pan, C. Song, J. Phys. Chem C, 2016, 120, 1633-1639.

[11] C. Daumont, J. Wolfman, C. Autret-Lambert, P. Andreazza, B. Negulescu, Appl. Phys. Lett. 2018, 112, 112401.

[12] D. Lee, S. H. Baek, T. H. Kim, J.-G. Yoon, C. M. Folkman, C. B. Eom, T. W. Noh, Phys. Rev. B, 2011, 84, 125305.

[13] A. Q. Jiang, C. Wang , K. J. Jin , X. B. Liu , J. F. Scott , C. S. Hwang , T. A. Tang , H. B. Lu, G. Z. Yang, Adv. Mater. 2011, 23, 1277–1281.

[14] Y. B. Lin, Z. B. Yan, X. B. Lu, Z. X. Lu, M. Zeng, Y. Chen, X. S. Gao, J. G. Wan, J. Y. Dai, J.-M. Liu, Appl. Phys. Lett., 2014, 104, 143503.

[15] Z. Chen, J. Liu, Y. Qi, D. Chen, S.-L. Hsu, A. R. Damodaran, X. He, A. T. N'Diaye, A. Rockett, L. W. Martin, Nano Lett., 2015, 15, 6506−6513.

[16] T. Gao, X. Zhang, W. Ratcliff, S. Maruyama, M. Murakami, A. Varatharajan, Z. Yamani, P. Chen, K. Wang, H. Zhang, R. Shull, L. A. Bendersky, J. Unguris, R. Ramesh, I. Takeuchi, Nano Lett., 2017, 17, 2825−2832.

[17] J. Wang, J. B. Neaton, H. Zheng, V. Nagarajan, S. B. Ogale, B. Liu, D. Viehland, V. Vaithyanathan, D. G. Schlom,U. V. Waghmare, N. A. Spaldin, K. M. Rabe, M. Wuttig, R. Ramesh, Science, 2003, 299, 1719-1722.

[18] G. Catalan, J. F. Scott, Adv. Mater., 2009, 21, 2463–2485.

[19] R. Uecker, B. Velickov, D. Klimm, R. Bertram, M. Bernhagen, M. Rabe, M. Albrecht, R. Fornari, D.G. Schlom, J. Cryst. Growth, 2008, 310, 2649-2658.

[20] F. Johann, A. Morelli, D. Biggermann, M. Arredondo, I. Vrejoiu, Phys. Rev. B, 2011, 84, 094105.

[21] Y. Qi, Z. Chen, C. Huang, L. Wang, X. Han, J. Wang, P. Yang, T. Sritharan, L. Chen, J. Appl. Phys, 2012, 111, 104117.

[22] Z. H. Chen, A. R. Damodaran, R. Xu, S. Lee, L. W. Martin, Appl. Phys. Lett., 2014, 104, 182908.

[23] K. M. Krishnan, A. R. Modak , C. A. Lucas, R. Michel, H. B. Cherry, J. Appl. Phys., 1996, 79, 5169.

[24] J. F. Mitchell, D. N. Argyriou, C. D. Potter, D. G. Hinks, J. D. Jorgensen, S. D. Bader, Phys. Rev. B, 1996, 54, 6172.

[25] K. Aoyagi, T. Kiguchi, Y. Ehara, T. Yamada, H. Funakubo, T. J. Konno, Sci. Technol. Adv. Mate., 2011, 12, S. 034403.

[26] H.W Jang, D. Ortiz, S-H Baek, C.M. Folkman, R.R. Das, P. Shafer, Y. Chen, C. T. Nelson, X. Pan, R. Ramesh, C-B Eom, Adv. Mat, 2009, 21, 817-823.

[27] C.T. Nelson, B. Winchester, Y. Zhang, S.-J. Kim, A. Melville, C. Adamo, C.M. Folkman, S.-H. Baek, C.-B. Eom, D.G. Schlom, L.-Q. Chen, X. Pan, Nano Letters., 2011, 11, 828–834.

[28] Y.-H. Chu, Q. He, C.-H. Yang, P. Yu, L. W. Martin, P. Shafer, R. Ramesh, Nano Lett., 2009, 9, 1726-1730.

[29] S. Farokhipoor, B. Noheda, J. Appl. Phys., 2012, 112, 052003.

[30] M. Hytch, F. Houdellier, F. Hue, E. Snoeck, Nature, 2008, 453, 1086 – 1090.

[31] S. K. Streiffer, C. B. Parker, A. E. Romanov, M. J. Lefevre, L. Zhao, J. S. Speck, W. Pompe, C. M. Foster, G. R. Bai, J. Appl. Phys., 1998, 83, 2742-2753.

[32] F. Kubel, H. Schmid, Acta Crystallographica. B, Structural Science, 1990, B46, 698-702.

[33] L. W. Martin, Y-H Chu, M. B. Holcomb, M. Huijben, P. Yu, S-J. Han, D. Lee, S. X. Wang, R. Ramesh, Nano Lett., 2008, 8, 2050-2055.

[34] H. Béa, M. Bibes, F. Ott, B. Dupé, X.-H. Zhu, S. Petit, S. Fusil, C. Deranlot, K. Bouzehouane, A. Barthélémy, Phys. Rev. Lett., 2008, 100, 017204.

[35] S. L. Dudarev, G. A. Botton, S. Y. Savrasov, Z. Szotek, W. M. Temmerman, A. P. Sutton, Phys. Stat. Sol. (a), 1998, 166, 429-443.

[36] L. V. Dobyeheva, P. L. Potapov, D. Schryvers Phys. Rev. B, 2004, 69, 184404.

[37] T-J. Park, S. Sambasivan, D. A. Fischer, W-S Yoon, J. A. Misewich, S. S. Wong, J. Phys. Chem. C, 2008, 112, 10359–10369.

[38] Y. H. Kim, A. Bhatnagar, E. Pippel, M. Alexe, D. Hesse, J. Appl. Phys., 2014, 115, 043526.

[39] R. Sæterli, S. M. Selbach, P. Ravindran, T. Grande, R. Holmestad, Phys. Rev B 2010, 82, 064102.

[40] A. P. Grosvenor, M. C. Biesinger, R. St.C. Smart, N. S. McIntyre, Surface Science, 2006, 600, 1771–1779.

[41] M. C. Biesinger, B. P. Payne, L. W.M. Lau, A. Gerson, R. St. C. Smart, Surf. Interface Anal., 2009, 41, 324–332.

[42] S. Oswald, W. Bruckner, Surf. Interface Anal. , 2004, 36, 17–22.

[43] D. Chen, Z. Chen, Q. He, J. D. Clarkson, C. R. Serrao, A. K. Yadav, M. E. Nowakowski, Z. Fan, L. You, X. Gao, D. Zeng, L. Chen, A. Y. Borisevich, S. Salahuddin, J.-M. Liu, J. Bokor, Nano Lett. 2017, 17, 486−493.

[44] J. T. Heron, J. L. Bosse, Q. He, Y. Gao, M. Trassin, L.Ye, J. D. Clarkson, C.Wang, Jian Liu, S. Salahuddin, D. C. Ralph, D. G. Schlom, J. Iniguez, B. D. Huey, R. Ramesh, Nature, 2014, 516, 370.

[45] J. Allibe, S. Fusil, K. Bouzehouane, C. Daumont, D. Sando, E. Jacquet, C. Deranlot, M. Bibes, A. Barthélémy Nano Lett., 2012, 12, 1141−1145.

Figures caption

Figure 1: a) Hysteresis cycles measured in zero electric field for different electrical states of the sample; b) I(V) curve.

Figure 2: RSM along the (a) $[103]_{pc}$, (b) $[-103]_{pc}$, c) $[013]_{pc}$ and (d) $[0\text{-}13]_{pc}$ BFMO directions. The corresponding orthorhombic direction is indicated for the GSO substrate peak in each map.

Figure 3: (a) TEM image of the whole stack; (b) SAED pattern of the stack (selected area added in the top right insert) along the $[100]_{pc}$ GSO zone axis; the bottom left insert shows the splitting of the high order spots indicated by the yellow box: the top blue spot corresponds to the substrate and the bottom red spots correspond to the PLD deposited layers; (c) and (d) Dark field TEM images obtained using the $(002)_{pc}$ and $(00\text{-}2)_{pc}$ diffracted beams for an un-poled region (c) and for a poled region (d).

Figure 4: (a) DFEH obtained using the $(00\text{-}2)_{pc}$ GSO diffracted beam; (b) Reconstructed ε_{yy} vertical deformation map; (c) Rotation map ω_{yx}; (d) Profile of the rotation angle measured along an horizontal line in the BFMO film, indicated by a black dashed line in figure (c); (e) schematics of the 4 domain variants in the BFMO film; (f) schematics of a possible domain structure around an 180° DW in zone A from figures (a) and (c); (g) schematics of a possible domain structure around the 109° DW in zone B from figures (a) and (c); (h) schematics of a possible domain structure in the zones C and D from figures (a) and (c).

Figure 5: HRTEM images of the BFMO / Ni interface in: (a) an un-poled region and (b) a poled region (yellow lines in (b) are just a guide for the eyes); O-K, Fe-L and Ni-L EELS profiles around the Ni/ BFMO interface in the: (c) un-poled region and (d) poled region (full lines). The dashed and dotted lines correspond to the weighed contributions to the O-K signal of O-K in BFMO and O-K in NiO, respectively; (e) O-K ELNES inside the BFMO film and at the Ni / BFMO interface for the un-poled and poled regions and for a NiO reference from the Digital Micrograph EELS Atlas.

Figure 6: (a) Survey XPS spectra for two electrodes in different electric states; (b) Spatial distribution of elements on both sides of the electrodes with respect to the analysis spot (18µm =blue zone); (c) Comparison of the high resolution spectra around the Ni $2p_{3/2}$ for different electric states; (d) High resolution spectra for the poled Ni$3p_{3/2}$ and the fit obtained using 5 peaks

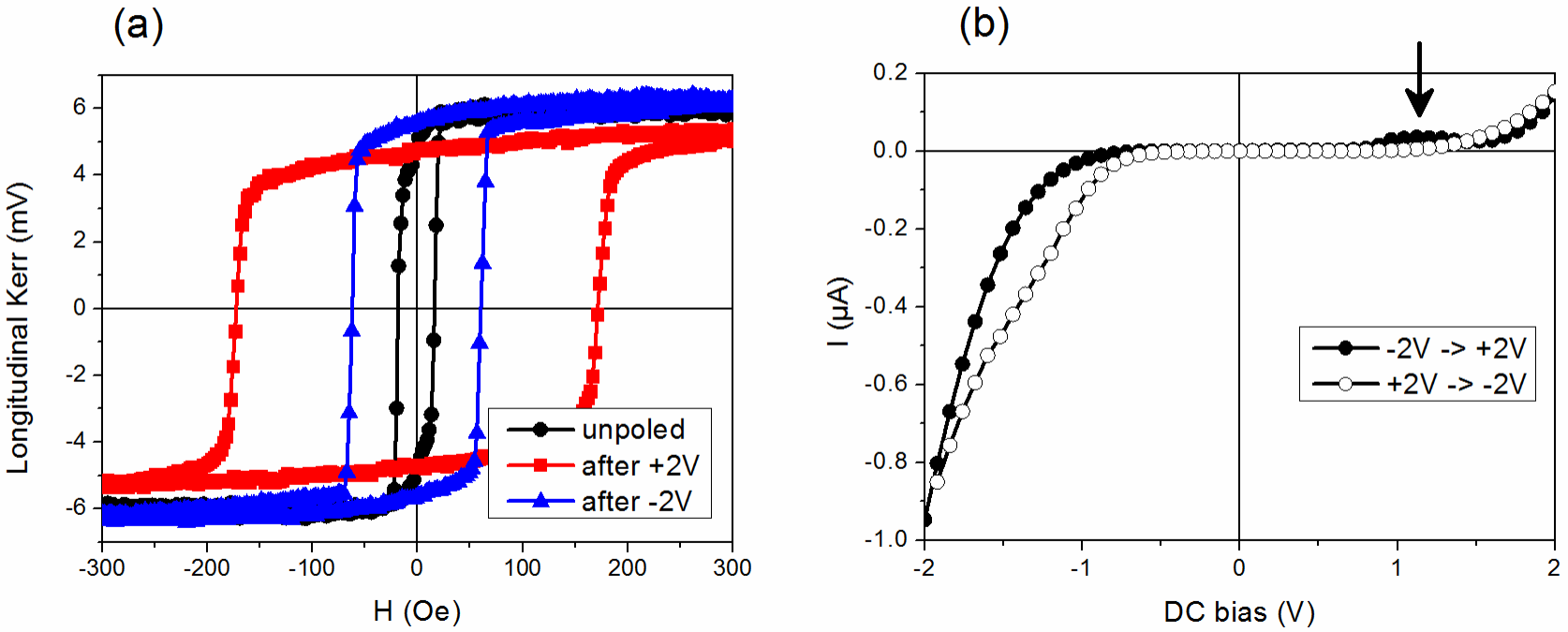
(a)
Longitudinal Kerr (mV)
H (Oe)
unpoled
after +2V
after -2V
(b)
I (μA)
DC bias (V)
-2V -> +2V
+2V -> -2V

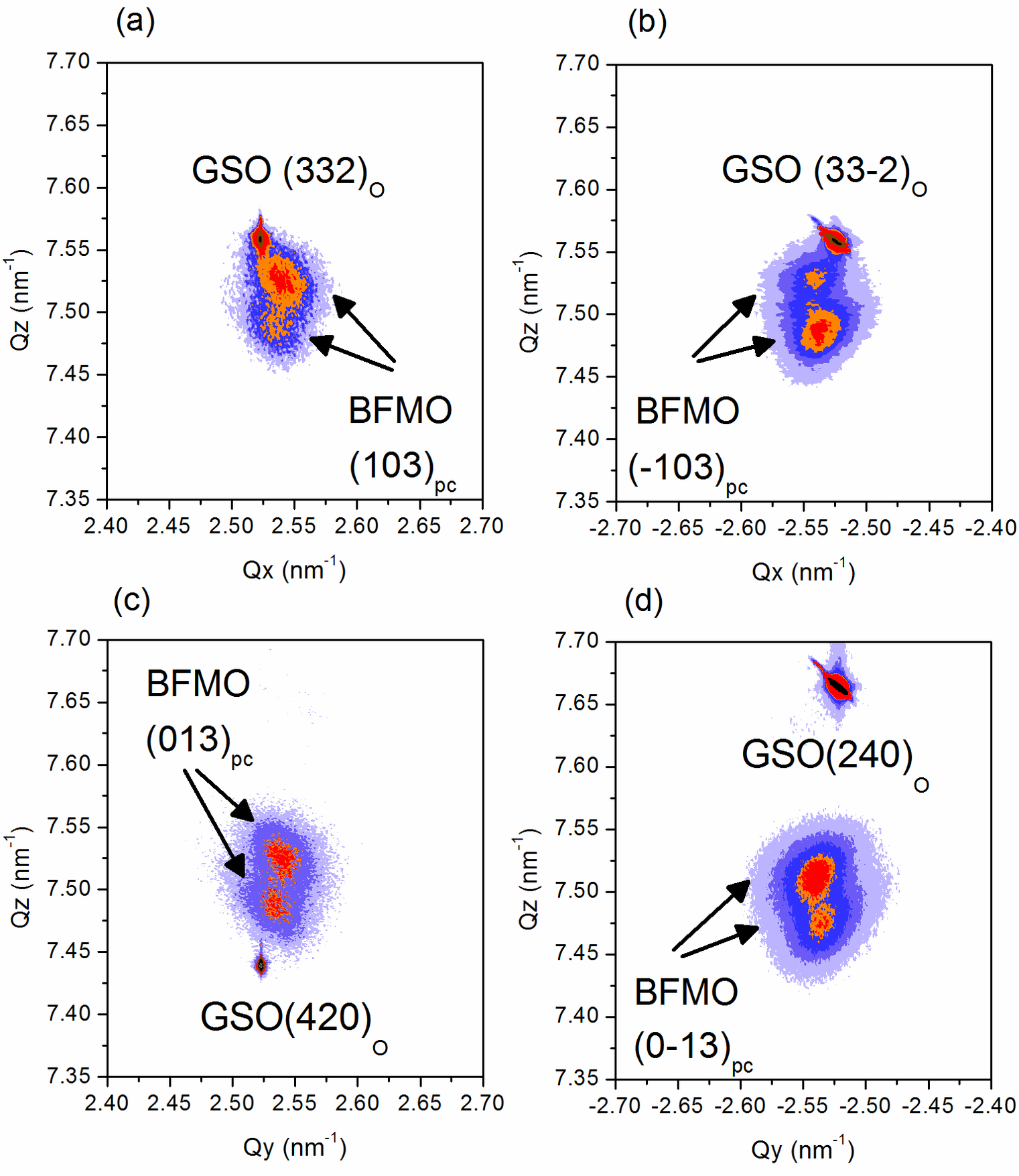
(a)
GSO (332)O
BFMO
(103)pc
Qz (nm-1)
Qx (nm-1)
(b)
GSO (33-2)O
BFMO
(-103)pc
Qz (nm-1)
Qx (nm-1)
(c)
BFMO
(013)pc
GSO(420)O
Qz (nm-1)
Qy (nm-1)
(d)
GSO(240)O
BFMO
(0-13)pc
Qz (nm-1)
Qy (nm-1)

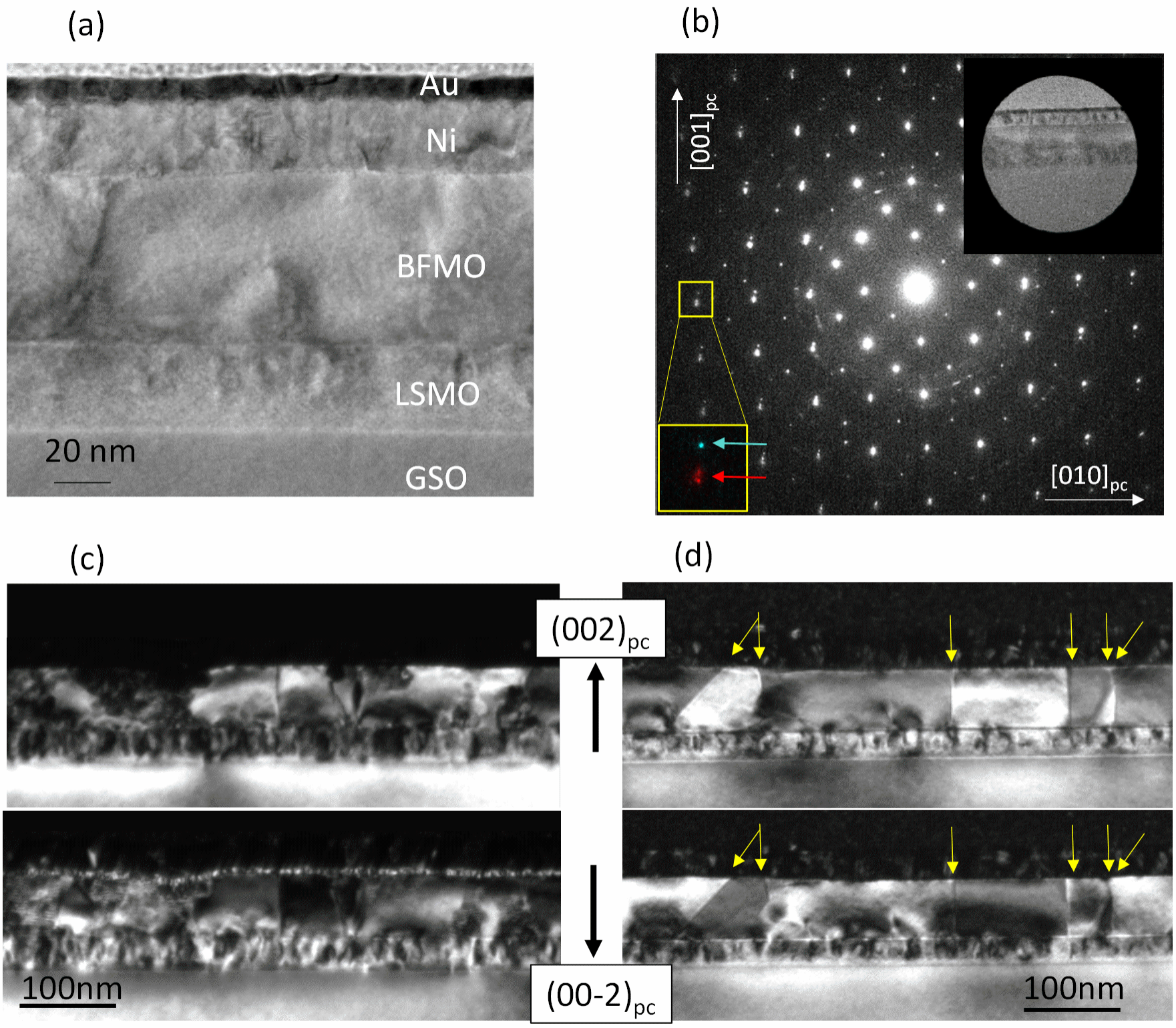
(a)
Au
Ni
BFMO
LSMO
GSO
20 nm
(b)
[001]pc
[010]pc
(c)
(002)pc
(00-2)pc
100nm
(d)
100nm

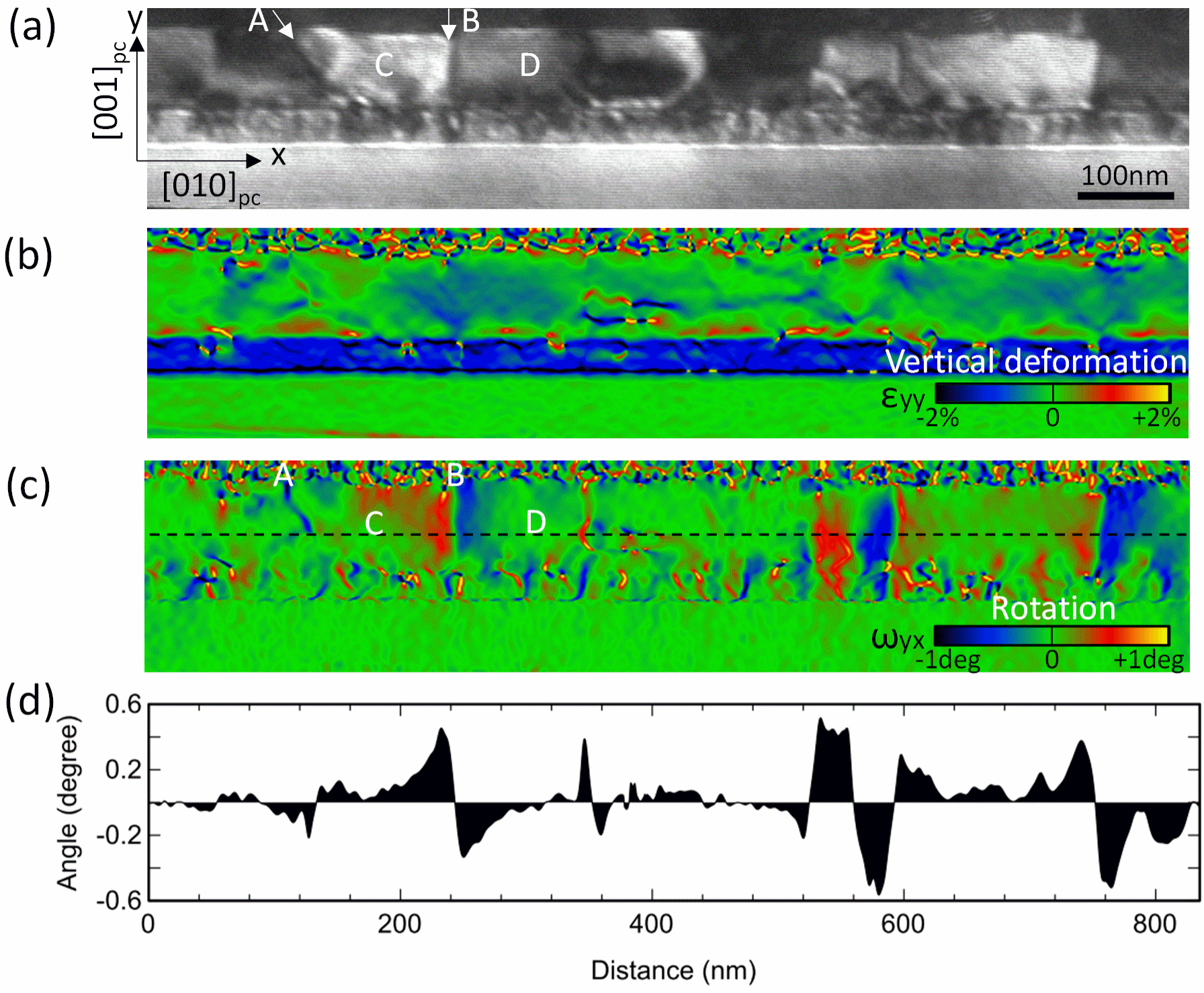
(a)
A
B
C
D
y
[001]pc
x
[010]pc
100nm
(b)
Vertical deformation
εyy
-2%
0
+2%
(c)
A
B
C
D
Rotation
ωyx
-1deg
0
+1deg
(d)
Angle (degree)
0.6
0.2
-0.2
-0.6
0
200
400
600
800
Distance (nm)
(e)
r2
r1
r3
r4
(f)
A
r2-
r2+
Substrate
(g)
B
r2-
r1+
+ω
-ω
(h)
C
D
r2-
r1+

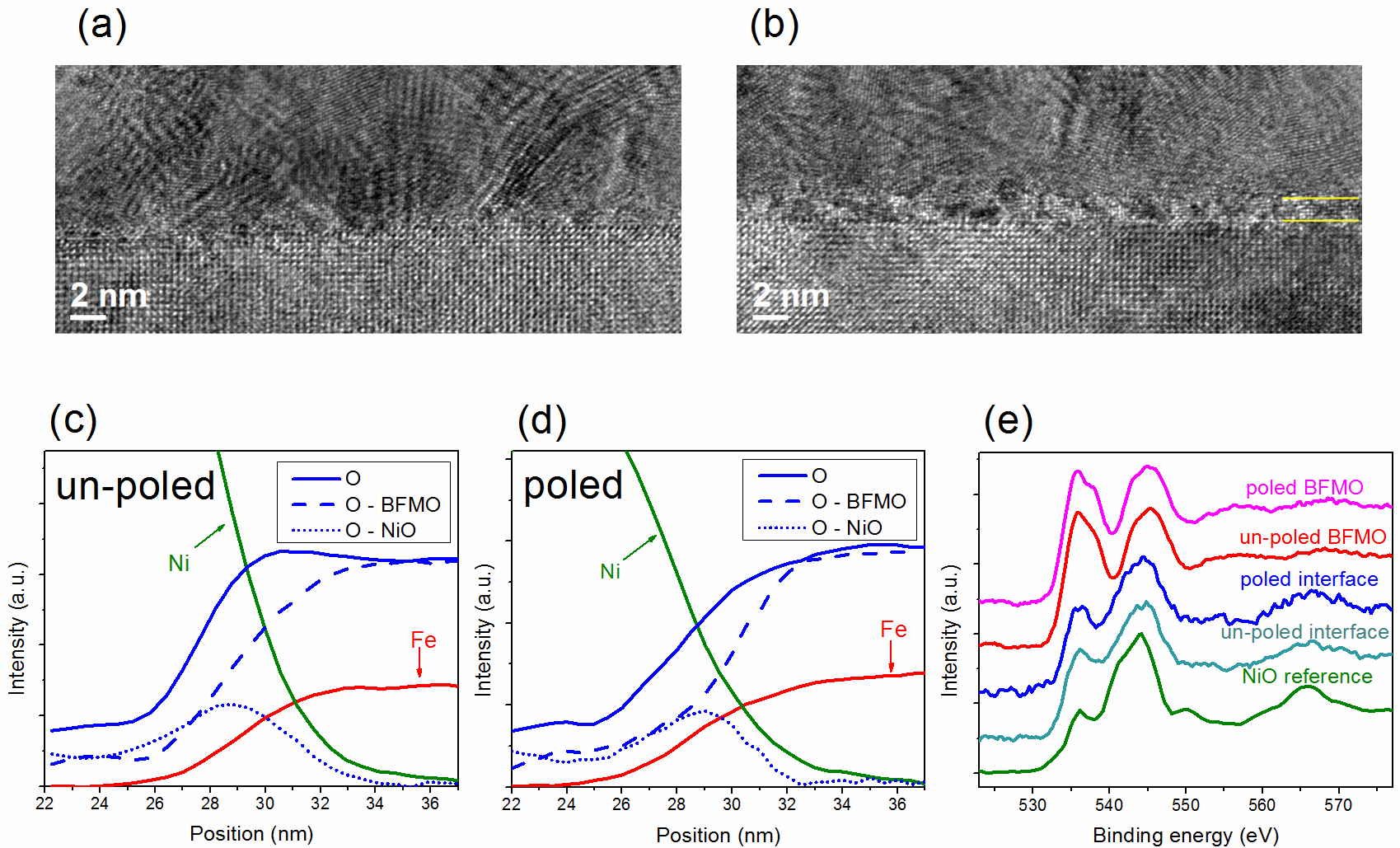
(a)
2 nm
(b)
2 nm
(c)
un-poled
O
O - BFMO
O - NiO
Ni
Fe
Intensity (a.u.)
Position (nm)
(d)
poled
O
O - BFMO
O - NiO
Ni
Fe
Intensity (a.u.)
Position (nm)
(e)
poled BFMO
un-poled BFMO
poled interface
un-poled interface
NiO reference
Intensity (a.u.)
Binding energy (eV)

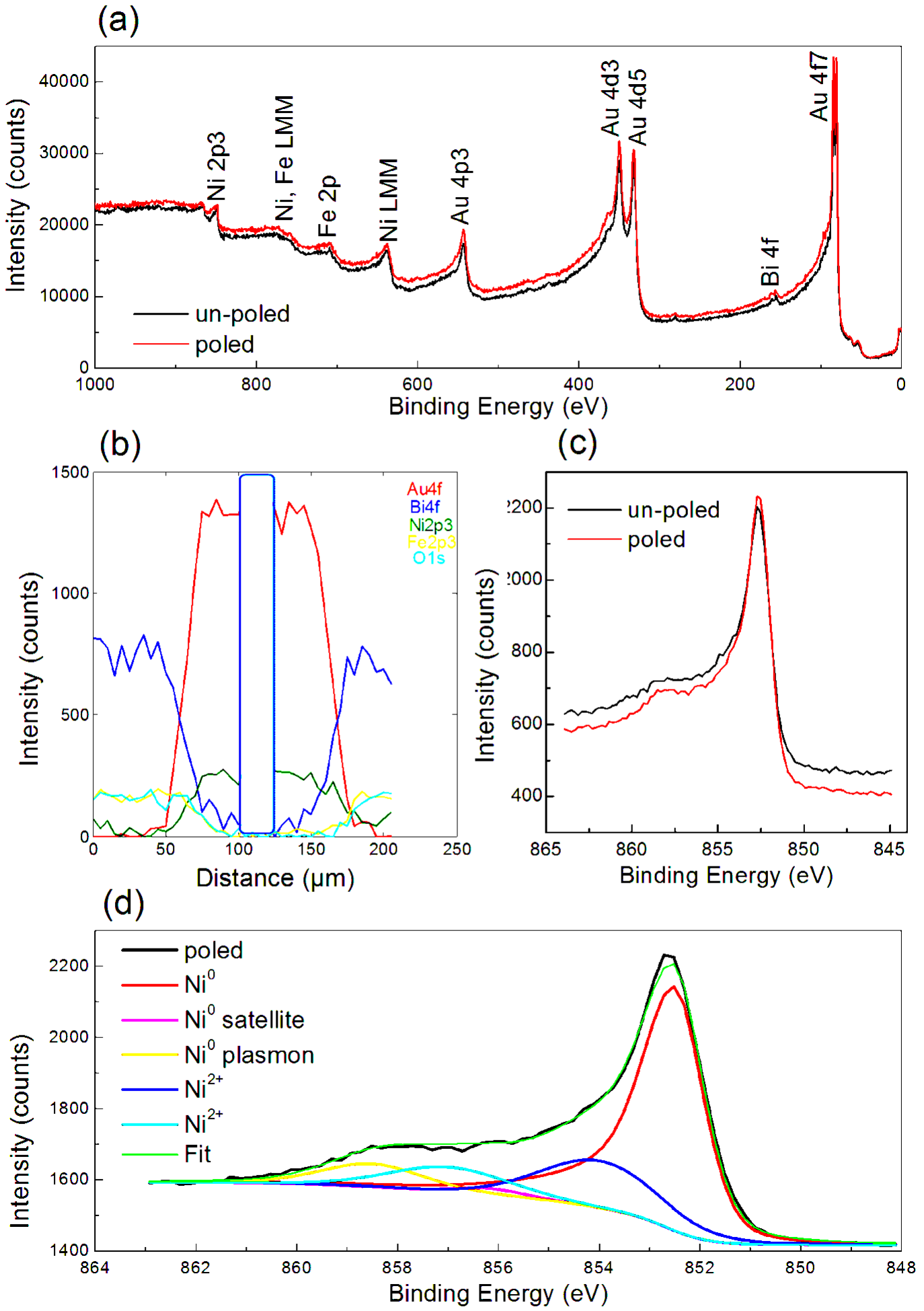
(a)
Intensity (counts)
Binding Energy (eV)
Ni 2p3
Ni, Fe LMM
Fe 2p
Ni LMM
Au 4p3
Au 4d3
Au 4d5
Bi 4f
Au 4f7
un-poled
poled
(b)
Intensity (counts)
Distance (μm)
Au4f
Bi4f
Ni2p3
Fe2p3
O1s
(c)
Intensity (counts)
Binding Energy (eV)
un-poled
poled
(d)
Intensity (counts)
Binding Energy (eV)
poled
Ni0
Ni0 satellite
Ni0 plasmon
Ni2+
Ni2+
Fit